J. Fluid Mech. (2007), *vol.* 577, *pp.* 105–126. © 2007 Cambridge University Press
doi:10.1017/S0022112006004502 Printed in the United Kingdom

Large-eddy simulation of a subsonic cavity flow including asymmetric three-dimensional effects

LIONEL LARCHEVÊQUE[1], PIERRE SAGAUT[2]
AND ODILE LABBÉ[3]

[1]IUSTI, Université Aix–Marseille I, UMR CNRS 6595, F-13453 Marseille, France
[2]Laboratoire de Modélisation en Mécanique, Université Pierre et Marie Curie – Paris 6,
case 162, 4 place Jussieu, F-75005 Paris, France
[3]ONERA, CFD and Aeroacoustics department, F-92322 Châtillon, France

(Received 22 February 2006 and in revised form 18 October 2006)

Large-eddy simulations of a cavity configuration yielding a mean flow that exhibits spanwise asymmetry are carried out. Results from the computations reveal that the asymmetry is due to a bifurcation of the whole flow field inside the cavity. It is demonstrated that the bifurcation originates in an inviscid confinement effect induced by the lateral walls. The branch of the bifurcation can be selected by slightly altering the incoming mean flow. Further investigations show that underlying steady spanwise modulations of velocity are amplified under the influence of the lateral walls. The modulation of the streamwise velocity component has the largest energy content and its dominant wavelength contaminates both vertical velocity and pressure. Complementary to these linear interactions, nonlinear energy transfers from streamwise velocity to pressure are also found. A transient analysis highlights the stiff transition from a symmetrical two-structure non-bifurcated flow to a stable unsymmetrical one-and-a-half-structure bifurcated flow. The switch to the bifurcated flow induces an alteration of the Rossiter aero–acoustic loop yielding a change in the dominant Rossiter mode and the appearance of a nonlinear harmonic of the first mode.

1. Introduction

1.1. *Context of the study*

Since the pioneering studies of Roshko (1955) and Karamcheti (1955), compressible flows over rectangular cavities have been known to exhibit strong velocity and pressure oscillations. Rossiter (1964) was the first to point out the key role of an aero–acoustic loop in the origin of these oscillations, similarly to many configurations exhibiting a shear layer impinging on an obstacle (see Rockwell & Naudascher 1979, for details). This description leads to the definition of a modal semi-empirical model, referred to as the Rossiter model, which has been successfully utilized to predict the discrete frequencies of the oscillations. Following Rossiter (1964), numerous studies have been devoted to cavity flows. The emphasis was mainly put on the improvement of both the understanding of the coupling and the refinement of its modelling, as described in the review articles by Rockwell & Naudascher (1978), Komerath, Ahuja & Chambers (1987) and Colonius (2001). Because the mixing layer and the pressure waves involved in the oscillations of the flow can be modelled with some success as two-dimensional to a first approximation, little attention has been paid to the influence of the spanwise direction on the structure of the flow inside the cavity. This restriction was supported until recently by some experimental (Ahuja & Mendoza 1995; Tracy & Plentovich 1997) and numerical Rizzetta (1988) studies demonstrating limited influence of the cavity width upon the level and frequency distribution of the Rossiter pressure modes. However recent advances in velocity measurements and in turbulence simulation tend to show that velocity field at least can be strongly modulated over the whole cavity because of the lateral boundaries. The purpose of this paper is to explore numerically the possible origin of such three-dimensional effects by focusing on a case strongly departing from two-dimensionality as described in the experimental study of a subsonic shallow cavity flow by Forestier, Geffroy & Jacquin (2000). Large-eddy simulation (LES) is used for such computations because of the quite large Reynolds number of the flow and the three-dimensional effects that are sought. Moreover, LES has been proved to accurately reproduce the features of compressible cavity flows found in experimental data, see Larchevêque *et al.* (2003) and Larchevêque *et al.* (2004).

1.2. *Three-dimensionality in cavity flows*

Three-dimensional effects inside a cavity were first reported by Maull & East (1963) for low-speed water flows. Wall visualizations based on viscous coating show the existence of stationary periodical cells in the spanwise direction whose number and size vary with the width of the cavity. An interesting point to note is that some of the pictures exhibited a non-symmetrical pattern with respect to the half-span line (or midpoint) of the cavity. Spanwise modulations have also been found inside the mixing layer by Rockwell & Knisely (1980). Visualizations using hydrogen bubbles reveal that, as well as the wavelength related to the classical ribs in the later stage of the layer, a larger wavelength roughly equal to the separation distance between two rolls is found upstream. The authors state that the large-scale recirculation vortex inside the cavity could be partly responsible for this spanwise modulation.

Indirect evidence of the three-dimensional nature of high-Reynolds-number cavity flows is found when looking at the ‘wake mode’ highlighted by Gharib & Roshko (1987) for a low-Reynolds-number axisymmetric shallow cavity. This specific mode of oscillation is due to the periodical ejection of part of the large recirculating vortices out of the cavity resulting in a huge increase of the drag. Two-dimensional direct numerical simulations (Rowley, Colonius & Basu 2002; Gloerfelt, Bailly & Juvé 2000) and Reynolds-averaged computations (Shieh & Morris 2000) were able to reproduce this phenomenon, while in their three-dimensional counterpart the classical ‘shear mode’ induced by the aero–acoustic coupling was recovered (see Gloerfelt *et al.* 2002, for details). Suponitsky, Avital & Gaster (2005) recently demonstrated that in a single computation transition from the ‘wake mode’ to the ‘shear mode’ can be achieved by enforcing the three-dimensionality of the flow by means of added three-dimensional perturbations. In a related way, Larchevêque *et al.* (2003) found that in an LES of a deep cavity flow with a spanwise homogeneous direction a reduced width of the computational domain induces a spurious recirculation vortex and alters the pressure spectra.

These observations tend to demonstrate that some intrinsic three-dimensional phenomena are at play inside the cavity that are complementary to the mixing layer–pressure wave coupling. Three-dimensional effects have been theoretically identified for other recirculating flows such as lid-driven cavity (Albensoeder, Kuhlmann & Rath 2001) and backward-facing step (Barkley, Gabriela m. Gomes & Henderson 2002).

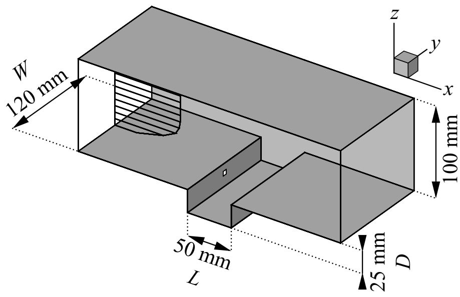

FIGURE 1. Geometrical description of the cavity within the wind tunnel. The rectangle located on the upstream wall of the cavity marks the location of the pressure sensor for both the experiments and the simulations. Length-to-depth ratio: $L/D=2$. Length-to-width ratio: $L/W=0.42$.

For the sake of completeness mention should also be made of the spanwise pure acoustic modes encountered in compressible cavity flows by Larchevêque *et al.* (2004) although their energy content is several orders of magnitude lower than that of the aero–acoustic Rossiter modes.

1.3. *Configuration studied and experimental results*

The geometry of the cavity and the flow parameters used in the present numerical study correspond to the experiments by Forestier *et al.* (2000). These authors have performed measurements of a flow with $M=0.8$ over a shallow cavity with ratio of length L to depth D equal to 2. The length of the cavity is 50 mm resulting in a length-based Reynolds number value of $Re_L=8.6\times 10^5$. The cavity was located in the ONERA S8B wind tunnel of cross-section 120 mm × 100 mm as described in figure 1, yielding a length to width W ratio of 0.42.

The measurement database includes fast-schlieren pictures, pressure spectra and mean as well as phase-averaged velocity fields in the vertical half-span and horizontal aperture planes obtained from laser Doppler velocimetry. The experimental apparatus and set-up were similar to the ones used in the deep cavity study by Forestier, Jacquin & Geffroy (2003), the main difference being a shift of the pressure sensor in the upward direction because of the decreased depth of the cavity. Details on the set-up can be found in that reference.

Pressure measurements and schlieren pictures reveal that the flow oscillates under the influence of the aero–acoustic coupling described by Rossiter. Moreover the dominant first mode of oscillation has frequency and level almost the same as the ones observed in the deep cavity by Forestier *et al.* (2003). Similarity in frequencies also occurs for higher modes. On the other hand, velocity fields differ noticeably: the oscillation loop only involves one vortex per cycle compared to the three vortices found for the deep cavity configuration. The most striking difference is found when looking at the spanwise distribution of velocity. While inside the deep cavity the flow away from the lateral boundary layers is close to homogeneity in the spanwise direction, the flow field related to the shallow configuration is strongly modulated over the whole width of the wind tunnel. Moreover, the spanwise velocity patterns do not exhibit symmetry with respect to the geometrical symmetry plane of the set-up.

This intriguing feature was the main motivation for performing LES of the configuration. Such computations take advantage of the knowledge gained from LES

Label	Subgrid model	Spanwise boundary condition	Initial forcing	Inflow forcing
MIL	MiLES	Wall	No	No
MS	Mixed scale	Wall	No	No
SMS	Selective mixed scales	Wall	No	No
MIL_{il}	MiLES	Wall	Left	No
MIL_{ir}	MiLES	Wall	Right	No
MIL_{l}	MiLES	Wall	No	Left
MIL_{r}	MiLES	Wall	No	Right
MIL_{s}	MiLES	Slip wall	No	No
MIL_{p}	MiLES	Periodicity	No	No

TABLE 1. Computational models.

previously performed by Larchevêque *et al.* (2003) related to the deep cavity case described in Forestier *et al.* (2003).

1.4. *Outline of the article*

The article is organized as follows: the numerical method and the parameters of the computations are briefly described in § 2. The meticulous validation process based on the use of the extensive experimental dataset of Forestier *et al.* (2000) is detailed in § 3. The last section is dedicated to the characterization of the spanwise asymmetry of the flow with discussions on its origin (§ 4.1), the influence of the inflow and lateral boundary conditions (§ 4.2) and an analysis of the space and time scales, both steady and unsteady (§ 4.3). Finally the major findings of the paper are summarized in § 5.

2. Numerical methods

The numerical method used for the present simulations is similar to the one used for the successful LES of the deep cavity configuration presented in Larchevêque *et al.* (2003). Therefore, it will not be detailed in the present paper. Two classes of computation have been carried out. The first one, classically referred to as MiLES, is based on an implicit subgrid modelling through the upwind optimized AUSM-type scheme proposed in Mary & Sagaut (2002). The second one relies on a classical LES with a second-order-accurate centred scheme coupled to the mixed-scale subgrid model in its standard or selective form (see Sagaut 2005 and Lenormand *et al.* 2000 for details). An hybridization with the upwind scheme is performed through the wiggle sensor proposed in Mary & Sagaut (2002) to avoid odd/even oscillations induced by purely centred schemes. The modelling strategies adopted in each of the simulations that have been carried out are listed in table 1 along with the labels used hereafter. Time integration is carried out by means of a standard third-order compact Runge–Kutta scheme.

Non-reflective boundary conditions are highly desirable for cavity flow simulations in order to prevent alteration of the aero–acoustic resonant loop. Moreover, realistic velocity profiles at the upstream edge of the cavity are required as a key parameter to accurately predict the growth of the mixing layer. A characteristic-based inflow condition coupled with synthetic turbulence generated through the addition of space-filtered and time-correlated random fluctuations, as described in Sagaut *et al.* (2004), is retained to fulfil these requirements. Both first- and second-order velocity statistical moments are set according to the experimental data. A subsonic characteristic-based condition is used at the outflow plane. A two-layer instantaneous wall function is

Cells	Δx^+ (streamwise)	Δy^+ (normal)	Δz^+ (spanwise)	Cells within δ_ω^0	Δt
39750×144 (spanwise)	$80 \sim 300$	$70 \sim 90$	$10 \sim 20$	10	1.4×10^{-7} s

TABLE 2. Typical cell characteristics and time step.

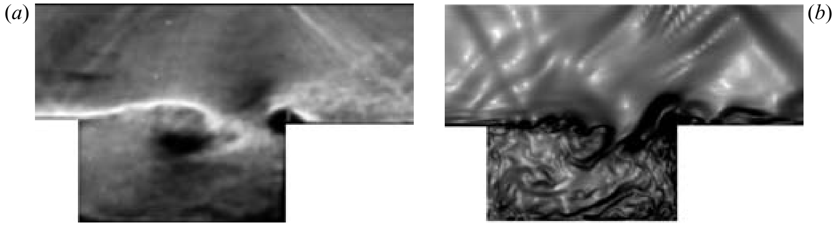

FIGURE 2. (*a*) Experimental fast schlieren view of Forestier *et al.* (2000) using a vertical knife and (*b*) filled isolevels of $\|\nabla\rho\|$ from the SMS computation.

used to make the computations feasible despite the small thickness of the boundary layer and the large dimensions of the wind tunnel that need to be discretized. For some computations frictionless wall and periodic boundary conditions have also been used.

The computational mesh is designed using the finest grid used for the deep cavity computation by Larchevêque *et al.* (2003) as a model. The inlet plane is located one cavity length L upstream of the cavity whereas the outflow boundary is $4L$ from it. As illustrated by figure 1, the upper wall of the wind tunnel is included in the computational domain and the lateral walls and their boundary layers are also taken into account because of the spanwise inhomogeneity of the flow revealed by the experiments. This yields a grid of nearly 6 millions cells whose features are described in table 2. According to the previous computations presented in Larchevêque *et al.* (2003), the number of cells contained in the vorticity thickness measured at the mouth of the cavity is more than large enough to allow an accurate capturing of the shear layer dynamics.

For all the computations, statistical data have been averaged over at least 50 periods of the first mode of oscillations.

3. Validation

Wind-described tunnel experiments in Forestier *et al.* (2000) have shown that for the present cavity the aero–acoustic Rossiter loop is the most energetic process. Therefore it is of importance to check the accuracy of its description by the numerical simulations. The use of strioscopic views is a qualitative way to do so. A comparison between pictures from the experiments of Forestier *et al.* (2000) in figure 2(*a*) and from the SMS simulation in figure 2(*b*) at a similar phase time shows that this computation is able to predict both the pressure wave pattern and the large vortex entering the cavity, here located near its mid-length point. Moreover the phase relation between the two phenomena is accurately reproduced. The MIL simulation yields a similar agreement with the experimental data while the MS one exhibits a lower density of pressure waves in the channel over the cavity.

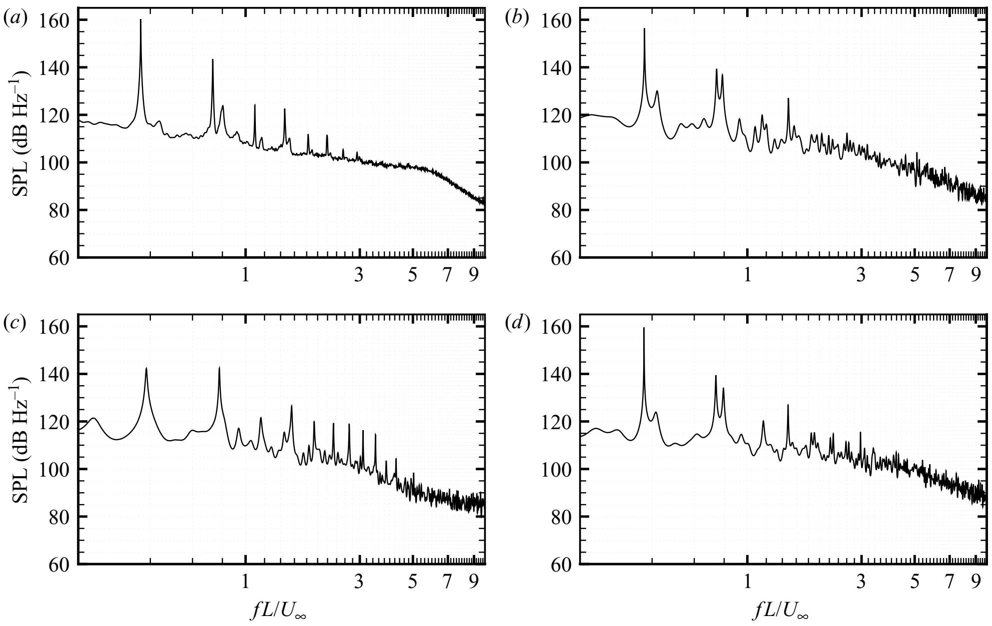

FIGURE 3. Power density spectra of pressure in sound pressure level (SPL) on the upstream wall at the location shown in figure 1: (*a*) experiment, (*b*) MIL, (*c*) MS and (*d*) SMS computations.

The analysis of the power spectra obtained from a pressure sensor located on the front wall of the cavity quantitatively confirms these trends. The MS spectrum of figure 3(*c*) fails to reproduce the details of the experimental one plotted in figure 3(*a*). The frequency of the main oscillating mode is reasonably correctly predicted but its power level is underestimated by 20 dB. Moreover, multiple spurious harmonics of the main peak are found. Similar harmonics were found experimentally and numerically for the $L/D=0.42$ cavity case. It was demonstrated by Forestier *et al.* (2003) and Larchevêque *et al.* (2003) that they originated from the coalescence of incoming and reflected waves inducing a low density of pressure waves similar to those observed for the MS computation. It is worth noting that the subgrid model of the MS computation results in turbulent viscosity levels higher than in the other simulation of the present study. However the alteration in the amplitude of the first mode is too large to be explained only by a direct dissipative effect induced by a larger turbulent viscosity on the propagating pressure waves. This is supported by the fact that the experimental schlieren picture of figure 2 is free from coalescence of pressure waves. This means that the aero–acoustic phase relation and, by extension, the aero–acoustic loop are different in the MS computation compared to the experiments.

Unlike to the MS case, MIL and SMS spectra plotted in figure 3(*b*, *d*) are in good agreement with the experiments up to $St=5$ with an error lower than 5 dB. The main discrepancy is an underprediction of the first Rossiter mode and its harmonics while the second Rossiter mode is overpredicted. Note that, owing to the large difference in sampling time between simulations and wind-tunnel experiments and the possible very-low-frequency modulations of the Rossiter modes encountered in cavity flows, theses discrepancies are not necessarily relevant.

To check the influence of the post-processing step, spectra are computed from parts of the experimental signal restricted to the same sampling duration of 50 periods of

Mode	St (th.)	%	St (exp.)			St (comp.)		SPL (exp.)			SPL (comp.)	
1	0.353	100	0.362	0.365	0.368	0.371	0.372	159.2	162.6	168.8	156.4	159.6
2 × 1	0.706	100	0.726	0.728	0.735	0.744	0.740	142.5	146.8	150.8	139.4	139.4
2	0.745	67	0.789	0.803	0.811	0.787	0.801	120.5	125.5	136.5	136.8	134.0
3 × 1	1.059	88	1.087	1.092	1.104	1.078	–	114.6	122.3	126.0	115.0	–
3	1.136	18	1.152	1.164	1.202	1.153	1.171	110.3	113.8	119.2	119.9	120.2
4 × 1	1.412	94	1.451	1.455	1.470	1.485	1.478	117.2	121.5	128.4	127.1	126.9
4	1.528	13	1.507	1.522	1.542	1.568	–	110.8	114.8	118.7	115.4	–

TABLE 3. Characteristics of Rossiter modes and their ith harmonics denoted by $(i+1)\times$. Theoretical Strouhal number St values are obtained from the semi-empirical Rossiter (1964) formula $St=(n-\gamma)/(M+\kappa^{-1})$ where n is the mode number and γ and κ are parameters varying with the L/D ratio. Following Larchevêque *et al.* (2003), values of $\gamma=0.098$ and $\kappa=0.57$ are retained for $L/D=2$. Experimental values are obtained by testing all the realizations of a 50-period signal extracted from the full 7500-period signal. Only realizations for which modes exhibit peaks whose amplitude is 4 dB higher than the background level are retained, the percentage of such realizations over all the realizations being given in the % column. For experimental values, left and right numbers correspond to the 99 % lower and upper boundaries of the density probability functions, the central ones being the most probable values. The first and second computational values are respectively from to the MIL and SMS simulations.

the first Rossiter mode as for the computational data. Probability density functions of frequency and amplitude are extracted for the various modes from all possible spectra to allow refined comparisons between the experiments and the two MIL and SMS computations. Results are summarized in table 3 by displaying the most probable values and the bounds of 99 % probability interval for the most energetic pressure modes identified in the spectra, namely the first Rossiter mode, its fourth first harmonics and the next three Rossiter modes.

It is seen from table 3 that the amplitudes of the pressure modes are strongly modulated over time with variations over 10 dB, especially for the second Rossiter mode which even becomes indistinguishable for about one third of the 50-period realizations. Taking into account the statistical bias induced by theses variabilities and the limited duration of the computations, it is found that the amplitudes predicted by the computations mostly fit the 99 % probability bounds although the underprediction of the amplitude of the first Rossiter mode and its first harmonic is slightly improved.

One may argue that because of the low-frequency competitive energy exchange between modes highlighted by Kegerise *et al.* (2004), amplitudes of modes may be correlated, therefore preventing selection of a realizable spectra by arbitrarily choosing amplitudes within probability bounds for each mode. The experimental spectra computed using 50 periods, which are the closest to the ones from the simulation when considering the three most energetic pressure modes, are extracted to alleviate this drawback. The resulting spectra are plotted in figure 4 jointly with their counterparts from simulations and the errors in the amplitude of the three dominant peaks are found to be lower than 2 dB. Consequently, it is concluded from figures 3, 4 and table 3 that both the MIL and SMS computations are able to accurately reproduce the Rossiter loop, making them appropriate for the physical analysis to come. The very low-frequency behaviour is beyond the scope of the present paper.

A similar better accuracy of the MIL and SMS simulations than the MS one is found by looking at the streamwise velocity profiles in the mid-span plane plotted in

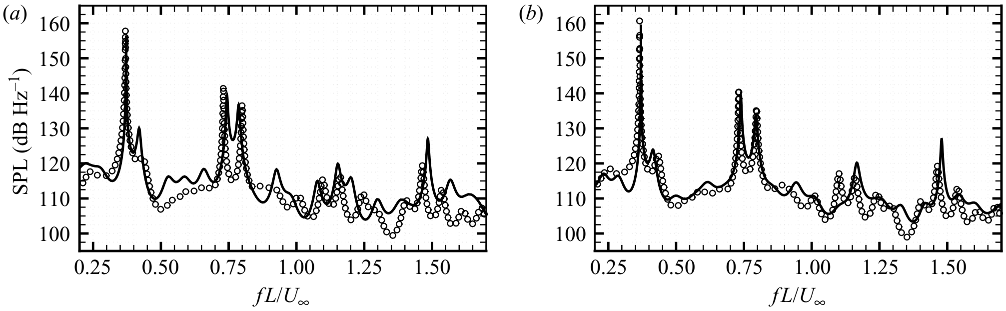

FIGURE 4. Power density spectra of pressure on the upstream wall at the location shown in figure 1: comparison between spectra obtained from computation (solid line) and the experimental spectra of the 50-period realizations best fitting the three most energetic peaks (circles); (*a*) MIL, (*b*) SMS.

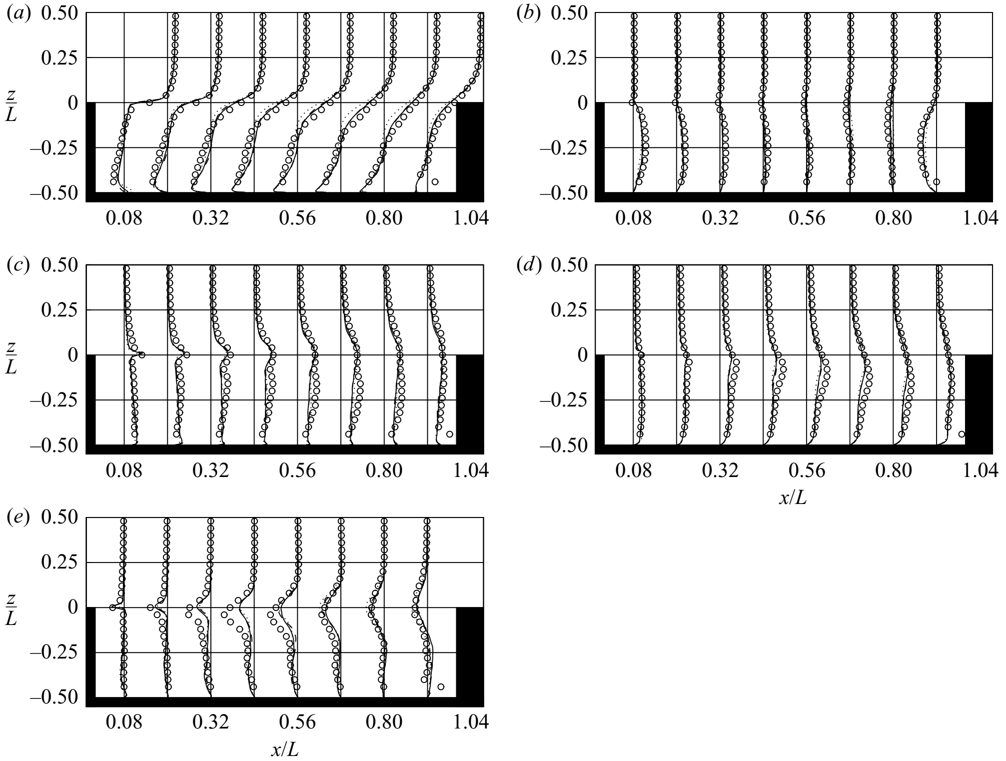

FIGURE 5. Velocity statistics in the mid-span plane of the cavity: (*a*) longitudinal mean velocity, (*b*) vertical mean velocity, (*c*) longitudinal fluctuating velocity, (*d*) vertical fluctuating velocity and (*e*) longitudinal–vertical Reynolds stress: ———, MIL simulation; ······, MS simulation; — — —, SMS simulation; ○, experiment.

figure 5(*a*). They indicate that the growth rate of the shear layer is underestimated in the MS simulation whereas MIL and SMS computations are in good agreement with the measurements except for a slight upward shift of the mixing layer centre. On the other hand, vertical velocity profiles are predicted equally well by all three simulations as seen in figure 5(*b*).

The turbulent fluctuations profiles of figure 5(c, d) are also in good agreement with the experiment for the inner part of the mixing layer. However levels are underpredicted inside the cavity from one-third of its length to the vicinity of the downstream wall. It is of interest to note that the double/single bumps in the experimental streamwise/vertical velocity profiles match the theoretical ones obtained from the mixing layer vortex model of Stuart (1967). A study of the phase-averaged data of Forestier *et al.* (2000) reveals that the higher levels found experimentally are due to the lone large vortex of the aero–acoustic loop gradually entering the cavity. Noting that this vortex is present in the simulations as seen in figure 2, it is suggested that the vortex is less coherent because of a greater three-dimensionality, as observed though in a milder form by Larchevêque *et al.* (2003) in the previous deep cavity computations.

The streamwise–vertical Reynolds stress profiles of figure 5(e) exhibit an overall good agreement between the experiment and the computations. Maximum levels are underpredicted near the half cavity length but are otherwise accurately predicted, being unaffected by the convection of the vortex as predicted by the model of Stuart (1967) that yields a zero cross-stress.

Although the velocity field is predicted well in the centre vertical plane the ability of the computations to reproduce the spanwise non-symmetric patterns has to be checked. Streamwise velocity and two-dimensional turbulent kinetic energy (TKE) maps of the horizontal aperture plane of the cavity are therefore presented in figure 6(a–d). They show that all the computations capture the quite complex highly non-symmetrical features of the flow though in an inverted form. Note that the flow fields from computations in figure 6(b–d) have been inverted with respect to the vertical plane $y/L = 1.2$ to make direct comparison with experimental results easier. A comparison of experiments and simulations shows that the streamwise velocity values are slightly underpredicted in figure 6(b–d) because of the aforementioned slight upward shift of the mixing layer.

The turbulent kinetic energy maps displayed in the right-hand parts of figure 6(a–d) show a similar inversion of the asymmetrical structure between the experiments and the three computations. Moreover, the low-mean-velocity regions also exhibit high TKE levels. This suggests that these areas correspond to a vertical extension of the recirculation zone beyond the cavity.

Finally note that the MS plots in figure 6(c) exhibit a spanwise structure bearing some similarity with those in MIL and SMS computations despite marked discrepancies in the pressure spectrum. This suggests that the asymmetry of the mean flow field may not be directly related to the aero–acoustic loop.

4. Asymmetry of the flow

4.1. *Origin*

It has been demonstrated in the previous section that the present computations are able to reproduce the asymmetry observed in the wind-tunnel experiments. Consequently this feature does not originate in flaws in the experimental set-up and therefore remains to be explained. The explanation is found in a preliminary LES that yielded a spanwise form of the asymmetry that was reversed compared to the three computations described in § 3.

A comparison between the first- and second-order statistics respectively coming from the preliminary simulation and from the SMS one shows that the two three-dimensional flow fields are mirror images of each other, inducing similar velocity

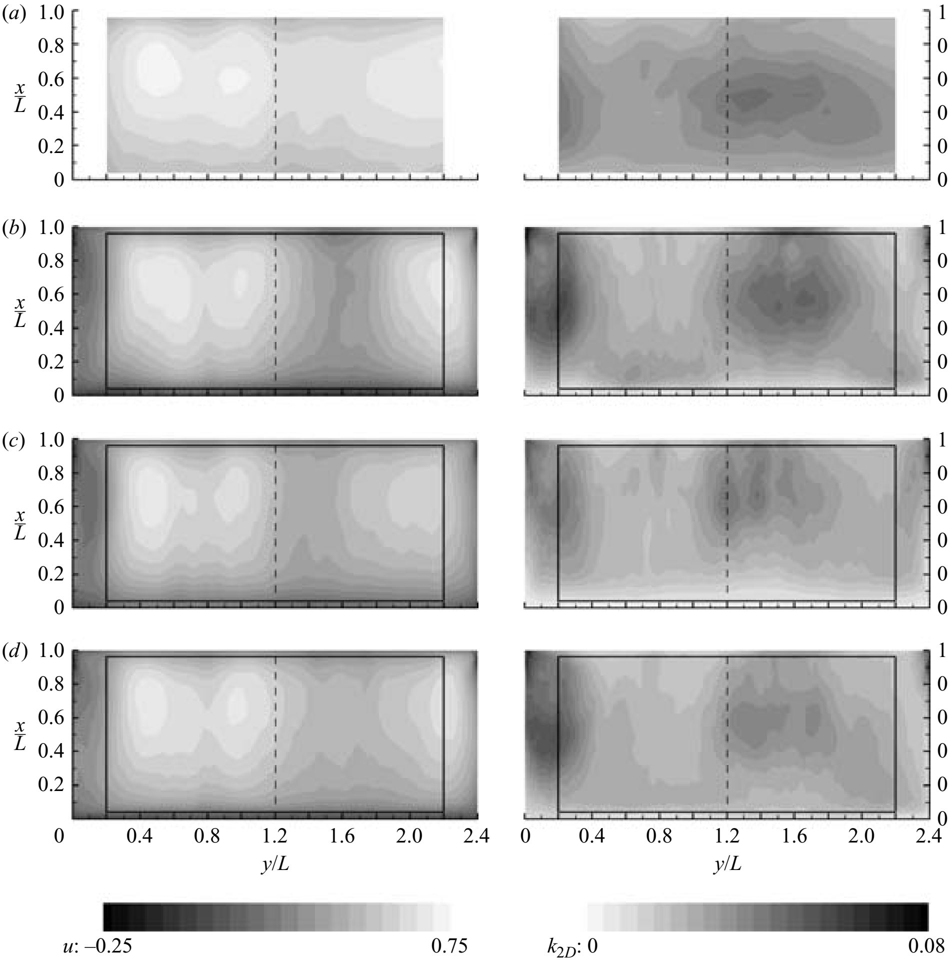

FIGURE 6. Streamwise velocity (left figures) and two-dimensional turbulent kinetic energy (right figures) maps in the horizontal aperture plane of the cavity; (*a*) experiment, (*b*) MIL, (*c*) MS and (*d*) SMS computations. Note that maps (*b*) to (*d*) have been inverted in the y-direction according to the formula $y'/L = 2.4 - y/L$.

profiles in the half-span vertical plane of figure 5 and reversed mean flow patterns in the horizontal plane of figure 6. It should be stressed that these two computations rely on the same computational parameters, including the mesh, numerical method and boundary conditions, with the exception of the turbulent fluctuations added to the mean velocity profile at the inflow plane. The fluctuations differ in their time series although their first- and second-order statistics are identical, implying that they are equivalent in a statistical sense. Statistically equivalent systems resulting in mirror image pairs are in fact the distinctive sign of a symmetry-breaking fork bifurcation.

4.2. *Sensitivity to external constraints*

Because of the spanwise symmetry of both the geometry and the mean boundary conditions, the two mirrored forms of the bifurcated flow field should be equally probable so as to yield the required spanwise symmetry for ensemble-averaged data over independent multiple realizations. However the experimental measurements that were collected and averaged over several measurement sessions do exhibit a marked asymmetry. This implies that there are either transient or spatial asymmetrical imperfections in the wind-tunnel flow field that always result in selecting the same branch of the bifurcation.

Auxiliary computations have been carried out to investigate the sensitivity of the bifurcation to various external constraints. Because the agreement of MIL simulation with the experimental measurements is similar to that of the SMS, all the computations described hereafter are carried out using the MiLES model in order to save computational time. Note that all these simulations rely on the same time series of inflow turbulent fluctuations as the MIL one for consistency reasons. The details of each of the computations are summarized in the five last lines of table 1.

The influence of asymmetrical history effects on the bifurcation is evaluated by altering the initial condition. The symmetry of the initial velocity profile $u^0(y,z)$ in the channel above the cavity is broken by adding a 1 % sinusoidal variation of the streamwise velocity component in the spanwise direction according to the formula:

$$u^0(y,z) = u^0_{sym}(y,z) \times f_{antisym}(y) = u^0_{sym}(y,z)\left[1 \pm 10^{-2}\sin\left(\frac{2\pi y}{W}\right)\right], \qquad (4.1)$$

with $u^0_{sym}(y,z)$ the fully spanwise-symmetric initial velocity field used in the previous computation. Two computations, denoted MIL_{ir} and MIL_{il}, are carried out starting from two antisymmetric initial flow fields. They are stopped after about 20 periods once it is obvious from the statistics that both of them yield the same pattern as for the previous MIL computation.

Next the possible effect of a spanwise inhomogeneity of the incoming flow field is addressed. The $\mathrm{MIL}_r/\mathrm{MIL}_l$ simulations rely on a right/left permanent alteration of the mean inflow velocity profile using the same 1 % antisymmetric modulation as for the cases with initial condition forcing. The right-hand forcing corresponds to a $-$ sign in the antisymmetric function of equation (4.1) whereas the left-hand forcing is obtained using the $+$ sign. Comparison between figures 7(*a*) and 7(*b*) shows that the flow fields resulting from MIL_r and MIL_l computation are antisymmetrical. This demonstrates that a constant low-amplitude asymmetry of the velocity as possibly found in wind tunnels allows the branch of the bifurcation to be selected.

A frictionless wall is substituted for the no-slip lateral walls in the MIL_s simulation in order to evaluate the influence of the lateral boundary layers on the bifurcation. Figure 7(*c*) shows that the spatial flow pattern remains almost unaltered even in the vicinity of the lateral wall, demonstrating that the bifurcation process does not originate in viscous effects induced by these walls.

Finally the lateral walls are totally suppressed and replaced by a periodic boundary condition in simulation MIL_p. Obviously the bifurcation process can no longer be sustained with such a boundary condition. The plots of figure 7(*d*) nonetheless reveal that a steady spanwise modulation of the flow still exists. Its amplitude is reduced compared to cases with bifurcation but the streamwise location of the maxima remains almost identical. The characteristic wavelength of this spanwise modulation is equal to half the width of the cavity and therefore is far too large to be related to transverse secondary instability of the mixing layer. An auxiliary conclusion is that, in flows with a periodic boundary condition, the computation of statistical averages over the periodic direction must be considered with great care since periodicity does not imply that the mean flow has no gradient in this direction.

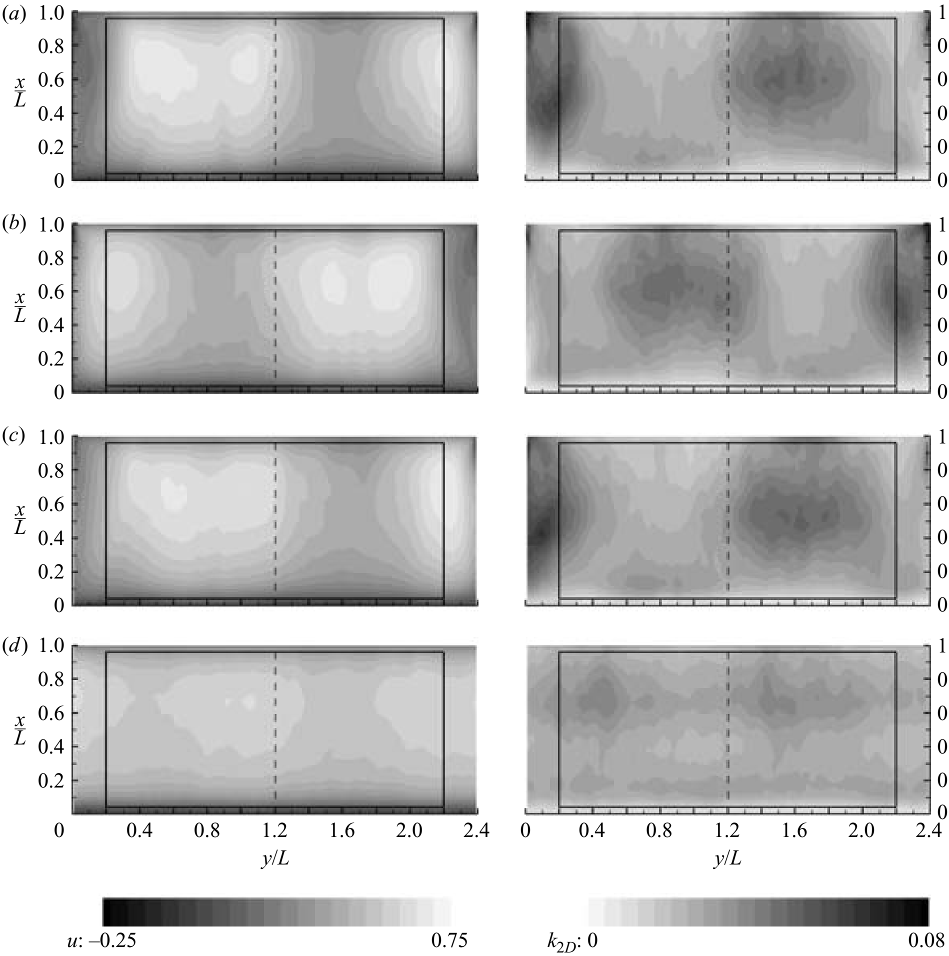

FIGURE 7. Streamwise velocity (left part) and two-dimensional turbulent kinetic energy (right part) maps in the horizontal aperture plane of the cavity: (*a*) MIL$_r$, (*b*) MIL$_l$, (*c*) MIL$_s$ and (*d*) MIL$_p$ computations.

Although the origin of the spanwise flow pattern is not clearly established, the steady structures observed in the MIL$_p$ computation reveal that the existence of lateral walls amplifies and constrains an underlying spanwise modulation of the flow to ultimately result in the bifurcation process. The next section is devoted to the analysis of the characteristic length and time scales of the bifurcated flow.

4.3. *Characteristic scales*

4.3.1. *Mean flow analysis*

The only available experimental velocity measurements in an horizontal plane correspond to the aperture of the cavity and consequently roughly to the centre of the mixing layer. It is therefore difficult to determine from them if the bifurcation is related either to only the mixing layer or to the recirculating flow inside the cavity. The vortical structures educed from the MIL$_r$ and MIL$_l$ mean flow field by means of the Q criterion (Hunt, Wray & Moin 1988) are shown jointly with the mean friction lines

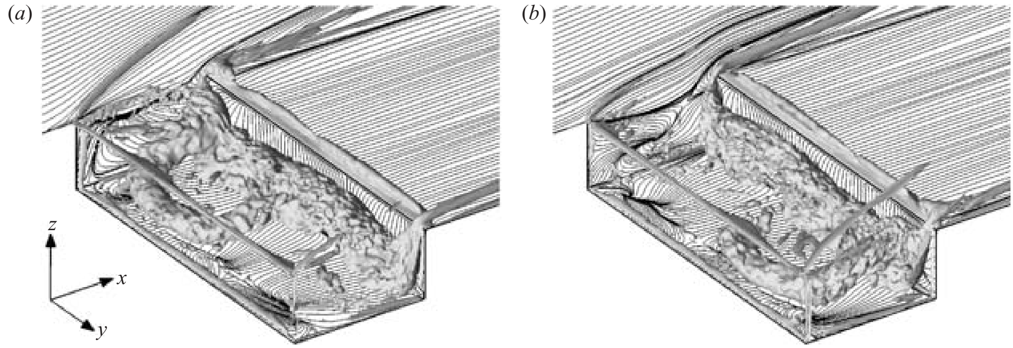

FIGURE 8. Mean friction lines and vortical structures educed using Q criterion of Hunt *et al.* (1988) with isosurfaces $Q = 2U_\infty^2/L^2$: (*a*) MIL$_r$ and (*b*) MIL$_l$ simulations.

in figure 8 to clarify this point. The plots reveal that the non-symmetrical pattern due to the bifurcation extents well beyond the mixing layer and is fully enantiomorphic.

The flow field inside the cavity exhibits the highest level of spanwise asymmetry. The main recirculation tube in the vicinity of the downstream wall is made slightly wavy and a large arch-shaped vortical structure that spans over more than half of the width of the cavity is found for $0.1 \lesssim x/L \lesssim 0.75$. Note that selecting a positive Q level half that in figure 8 shows an additional weaker, semi-arch-shaped structure of width roughly equal to $W/4$ that fills part of the remaining free span space. The semi-arch leans on the span wall, resulting in the skin friction line focus seen on the background wall in figure 8(*b*). The friction line arrangement on the lateral walls reveals that the mixing layer is deflected upward near the wall closest to the full-arch structure, presumably because of blocking effects due to this structure. The effect is strong enough to induce on this side a separation of the flow before the upstream corner. Corresponding, the wake structures beyond the downstream corner are weakened. It should be noted that the friction line pattern on the floor of the cavity bears some resemblance to some viscous coating visualizations by Maull & East (1963) related to incompressible cavity flows.

An analysis of sole figure 8 yields crude estimations of the length scales of the flow in the spanwise direction. One way to obtain a more accurate evaluation of these length scales is to perform spanwise space Fourier transforms of the mean flow field inside the cavity. The spanwise spectra are computed using the Lomb (1976)–Scargle (1982) method for unevenly spaced samples because of the clustering of the mesh near the lateral walls.

The method is used to obtain the longitudinal evolution of spanwise spectra along the line $z = L/4 = D/2$ roughly corresponding to the horizontal symmetry plane of the mean structures highlighted in figure 8. Evolutions are displayed for MIL, MIL$_s$ and MIL$_p$ computations respectively in figure 9(*a–c*). Streamwise velocity u, spanwise velocity v, vertical velocity w and pressure p spanwise spectra are plotted for each case. Note that SMS computation spectra are not shown here because of their similarity with MIL simulation ones.

Highest spectral densities are found for the streamwise velocity near $x/L = 0.45$. Each computation nonetheless exhibits a marked peak with a constant wavenumber over the whole longitudinal line. However the values of the peak wavenumber are computation-dependent, corresponding to wavelength values of $0.8W$ for both the MIL and MIL$_s$ simulations and $0.5W$ for the MIL$_p$ simulation. The same length scale

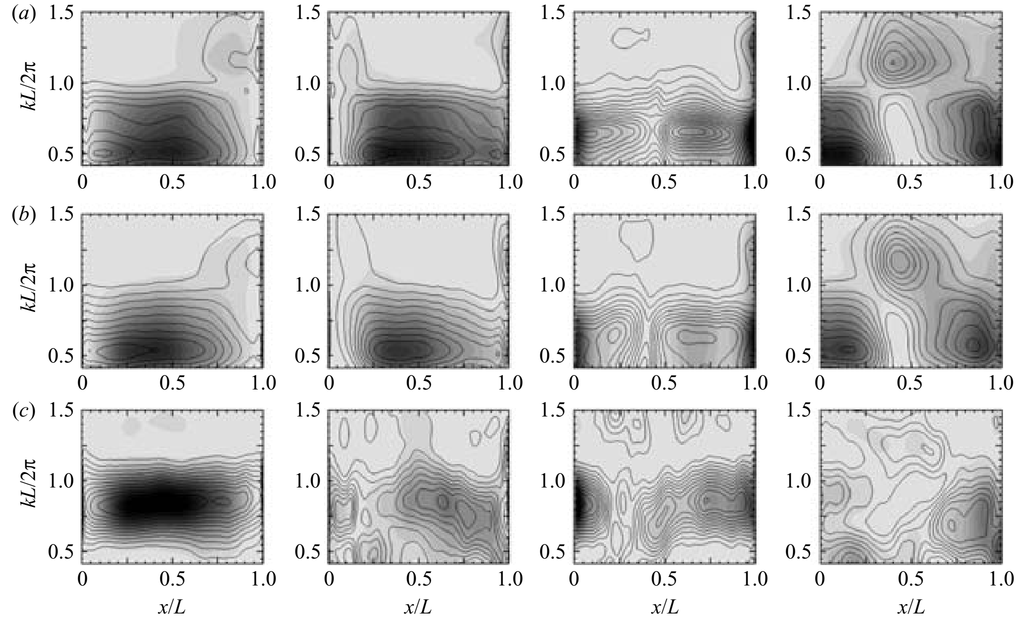

FIGURE 9. Longitudinal evolution of wavenumber spectra in the spanwise direction for height $z = L/4$; from left to right, levels for longitudinal, spanwise and vertical velocities and pressure: (a) MIL, (b) MIL_s and (c) MIL_p computations. Solid line isocontours correspond to spectral densities normalized by the local spanwise variance value. Background greyscale isocontours correspond to unnormalized spectral densities. Note that unnormalized levels have been multiplied by a factor of 10 in plot (c) compared to plots (a, b).

of $0.5W$, though less predominant, is also found in the MIL_p spectra of figure 9(c) for the spanwise and vertical velocity. On the other hand the MIL_p pressure spectra hardly exhibit any organization. This seems to indicate that pressure is not directly involved in the three-dimensionalization of the flow.

Spanwise velocity spectra of simulations including span walls (second column of figures 9(a, b) exhibit a dominant common wavelength of about $0.65W$. A common dominant wavelength is also seen in vertical velocity spectra from simulations MIL and MIL_s with a value of $0.8W$, similar to the one found for the streamwise velocity. Moreover the locations of u and w spectrum maxima are very close to each other as shown in figure 9(a, b), thus demonstrating that the spanwise modulations of these two velocity components are related.

The fourth plots of figure 9(a, b) show that for the MIL and MIL_s computations the streamwise velocity seems also to impose its dominant wavelength on the pressure spectrum over the first quarter and the last third of the cavity. In the central region, a shorter wavelength equal to $0.35W$ dominates but exhibits much lower peak values.

In addition to the collection of statistical data, time series of velocity components and pressure have been obtained along various lines inside the cavity for both the MIL_r and MIL_l computations. These data are useful to compute spanwise cross-spectra and bispectra between velocity and pressure by taking advantage of the time dimension to obtain a fully converged spectral estimator. Details on the definition of coherence and bicoherence functions extracted from the cross-spectra and bispectra can be found in Larchevêque *et al.* (2004).

The spanwise coherence spectra of figure 10 confirm that for MILES computations including span walls the vertical velocity and, to a lesser extent, the pressure are

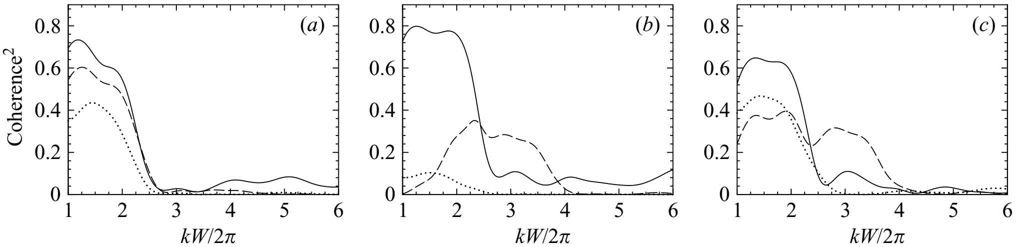

FIGURE 10. Spectra of spatial squared coherence at locations: (*a*) ($x/L=0.25, z/L=-0.25$), (*b*) ($x/L=0.5, z/L=-0.25$) and (*c*) ($x/L=0.75, z/L=-0.25$): ······, longitudinal velocity–spanwise velocity; ———, longitudinal velocity–vertical velocity; — — —, longitudinal velocity–pressure.

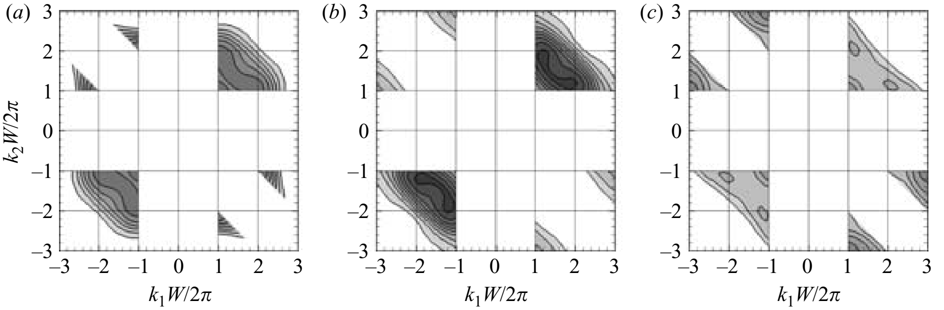

FIGURE 11. Spectra of $u \times u \leftrightarrow p$ spatial squared bicoherence with levels ranging from 0.1 (approximate threshold of significance) to 1 with incremental steps of 0.05; (*a*) ($x/L=0.25, z/L=-0.25$), (*b*) ($x/L=0.5, z/L=-0.25$) and (*c*) ($x/L=0.75, z/L=-0.25$). The regions corresponding to sum of wavelengths larger than the width of the cavity have been blanked.

highly correlated with the longitudinal velocity at a wavelength equal to $0.8W$. Lower levels of squared coherence are found between streamwise and spanwise velocity at the wavelength of $0.65W$ corresponding to the dominant mode of spanwise velocity as seen in figure 9(*b*, *c*). Note that the coherence between streamwise velocity and pressure is lower near the downstream wall than near the upstream wall, which is further evidence that the three-dimensionality of the mean flow is not induced by the aero–acoustic loop. In the central region of the cavity, the pressure is only moderately correlated with streamwise velocity for the wavelength $0.35W$ of the locally dominant pressure mode.

This mode nonetheless originates in an interaction between the velocity and pressure fields but in a nonlinear way as demonstrated by the ($u \times u$, p) spanwise bispectra plotted in figure 11(*a–c*) respectively related to locations ($x/L=0.25, z/L=-0.25$), ($x/L=0.5, z/L=-0.25$) and ($x/L=0.75, z/L=-0.25$). It is seen from figure 11(*b*) that in the centre of the cavity the squared bicoherence spectrum exhibits levels higher than 0.5 for a quadratic interaction between the dominant velocity mode of wavelength $0.8W$ and a velocity mode of lower wavelength, resulting in an energy transfer toward the aforementioned pressure mode of wavelength $0.35W$. Nonlinear interactions exist outside the centre region (see figure 11*a*, *c*) but they weakly involve velocity modes of lower energy content thus resulting in an indiscernible low-energy pressure mode.

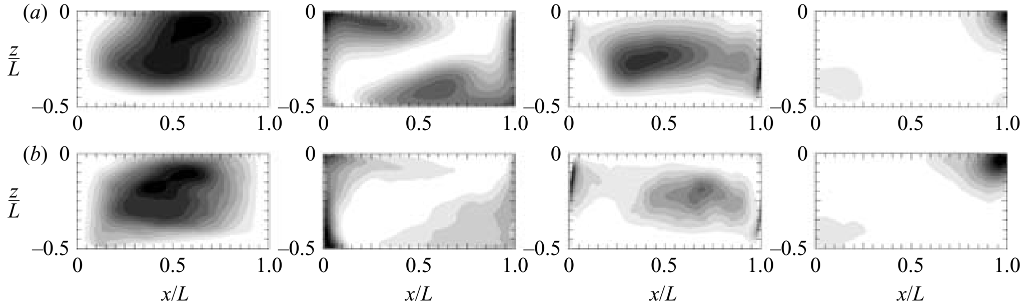

FIGURE 12. Streamwise-vertical map of the normalized energy content of the dominant spanwise mode; from left to right, levels for longitudinal, spanwise and vertical velocities and pressure: (*a*) MIL computation with wavenumbers ($k_u^* = k_w^* = 1.22, k_v^* = 1.51, k_p^* = 1.2$) and (*b*) MIL$_p$ computation with wavenumbers ($k_u^* = k_v^* = k_w^* = k_p^* = 2.0$).

Since the overall dominant modes are clearly identified for every computation and variable, it is of interest to consider the cavity map for the energy content of the dominant spanwise modes. Only maps for MIL and MIL$_p$ are shown respectively in figure 12(*a, b*) because the MIL and MIL$_s$ computations yield mostly similar results. Despite quite different wavenumbers, streamwise velocity dominant modes exhibit a very similar organization: maxima are found in the central region of the cavity and up to the mixing layer at $x/L = 0.6$, thus explaining the pattern seen in figures 6(*c*) and 7(*d*). The same remark holds for spanwise velocity maps except for an area near the floor of the cavity for $0.45 \lesssim x/L \lesssim 0.7$ found only for the case with bifurcation (figure 12*a*).

A study of the energy content of the vertical velocity reveals more marked differences between the computations. For the MIL computation, the location of maximal energy matches the central zone of high levels of the dominant streamwise mode, while for the non-bifurcated simulation MIL$_p$ the respective maxima of the vertical and streamwise modes are spatially uncorrelated. Lastly, plots of the energy content of the dominant pressure mode show that the region in which the interaction between the spanwise-modulated three-dimensional vortices contained in the mixing layer and the downstream edge is the main source of three-dimensionality for pressure. However the three-dimensionality does not radiate outside this restricted zone. Therefore it seems unable to trigger the streamwise velocity three-dimensionality via the Rossiter aero–acoustics loop.

To summarize the results of this section, the velocity field is modulated by spanwise modes of almost constant wavelength over the whole cavity. These characteristic wavelengths are altered by the bifurcation process, except for the spanwise velocity. Simulations SMS, MIL and MIL$_s$ exhibit similar streamwise modulations with a high level of linear correlation between velocity components u and w and, to a certain extent, pressure p, resulting in a unique characteristic wavelength for all of these three modes. Nonlinear energy exchanges nonetheless exist between velocity and pressure fields. They eventually yield a sustained secondary pressure mode in the central part of the cavity.

4.3.2. *Time-dependent analysis*

The time series of velocity components and pressure obtained along various lines inside the cavity for both the MIL$_r$ and MIL$_l$ computations have been sampled over a

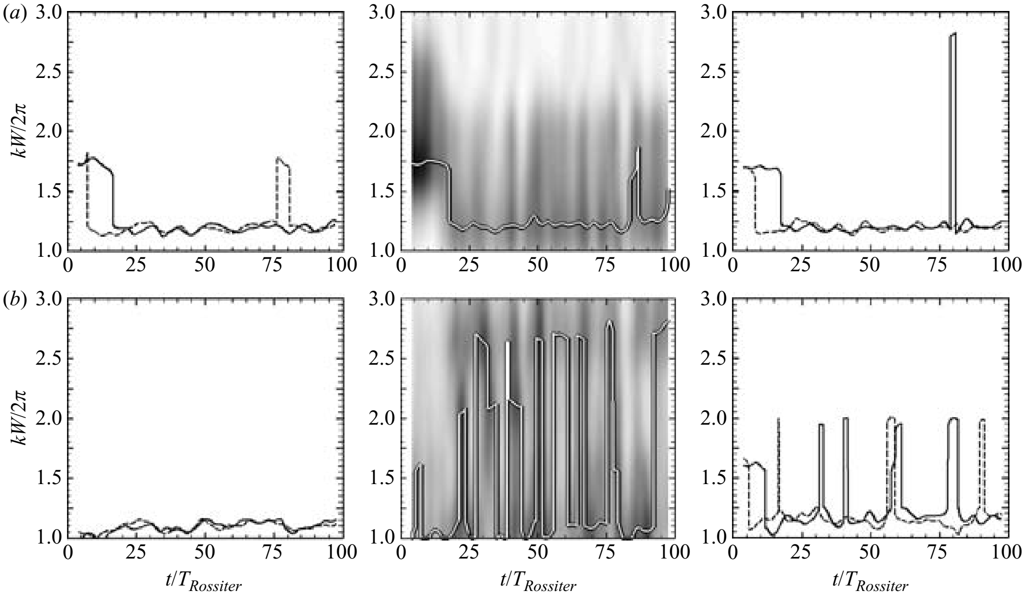

FIGURE 13. Time evolution of (a) streamwise velocity and (b) pressure dominant spanwise spatial mode in the — — —, MIL$_r$ and ———, MIL$_l$ computations at locations $x = L/4$ (left), $x = L/2$ (centre) and $x = 3L/4$ (right); for the $x = L/2$ plots, only curves from the MIL$_l$ computation have been drawn and they are superimposed on the time–wavenumber spectra used to compute them.

duration of about 100 periods of the first Rossiter mode once the aero–acoustic loop is established. This allows the identification of both the possible time modulations of the spanwise modes and the influence of the bifurcation process on the aero–acoustic oscillations.

These datasets are first used to check if the spanwise modulations of constant wavelengths highlighted in the previous mean flow analysis are subject to intermittency effects. To this end, instantaneous spanwise spectra are computed using the method described in § 4.3.1 and are smoothed using a Gaussian temporal sliding window to reduce statistical uncertainty. This method is applied at the three locations along the line $z = L/4$ previously used in § 4.3.1.

The resulting time–spanwise wavenumber spectra at location $x = L/2$ are displayed on the central plot of figure 13(a, b) respectively showing to streamwise velocity and pressure from the MIL$_l$ computation. The time evolution of the instantaneous dominant mode extracted from the spectra is superimposed on the plots and these curves clearly highlight two distinct regions to either side of $t/T_{Rossiter} \simeq 18$. Beyond that time, wavelengths extracted from the steady analysis (see figure 9) are recovered though with some intermittency for the pressure. On the other hand streamwise velocity and pressure wavelengths seen prior to that time are lower and almost equal to each other, bearing therefore some similarities with the ones obtained when considering the non-bifurcated MIL$_p$ computation. Consequently $t/T_{Rossiter} \simeq 18$ is identified as the bifurcation time.

For clarity and brevity, only the evolution of the instantaneous dominant modes at locations $x = L/4$ and $x = 3L/4$ are shown on the left and right plots of figure 13(a, b) for both MIL$_r$ (dashed line) and MIL$_l$ (solid line) computations. The MIL$_l$ plots of figure 13(a) demonstrate that roughly the same bifurcation time is recovered over the

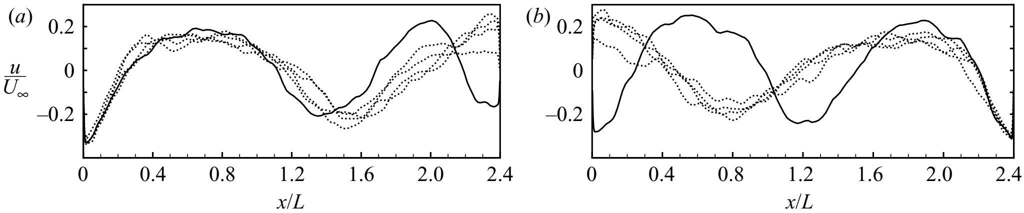

FIGURE 14. Profiles of short-time-averaged streamwise velocity along the spanwise line ($x = L/2, z = -L/4$): (*a*) MIL$_r$ and (*b*) MIL$_l$ computation; ——, $t/T_{Rossiter} \in [0, 9]$, · · · · · ·, $t/T_{Rossiter} \in [25, 34]$, [45, 54], [65, 74] and [85, 94].

whole cavity area even for pressure at location $x = L/2$ despite a milder transition. The same conclusions hold for the MIL$_r$ computation though the bifurcation is anticipated compared with the MIL$_l$ simulation with $t/T_{Rossiter} \simeq 9$. Focusing on the pressure, the lack of intermittency far from the downstream corner whereas close to it the intermittent wavelength is roughly equal to a submultiple of the full width, and the fact that the intermittency characteristic time is less than a few $T_{Rossiter}$, suggest that these features could be due to the forcing by pressure waves emitted from the downstream edge because of the Rossiter aero–acoustic coupling.

Short-time-averaged profiles along the spanwise line ($x/L = 0.5, z/L = 0.25$) of high spanwise velocity variance are computed to ensure that the bifurcation found in figure 13 is indeed related to the transition from the symmetric non-bifurcated case to the symmetry-breaking bifurcated one. The instantaneous streamwise velocity is averaged over $9T_{Rossiter}$ from the beginning of the data storage and from four equidistant times in the bifurcated time zone. The resulting profiles are plotted in figure 14(*a, b*) for the MIL$_r$ and MIL$_l$ computations, respectively. Comparison of the solid line with the dotted curves, respectively related to the averaging in the first and second time regions, highlights a dramatic change in the spanwise structure of the flow. Moreover, the solid line of figure 14(*b*) clearly exhibits a symmetrical pattern while mirrored dotted lines compare with those in figure 14(*a*). This demonstrates that the bifurcation time highlighted in figure 13 is associated with the breakdown of the symmetry of the mean flow.

The time at which the bifurcation occurs being known, it is of interest to evaluate the potential impact of the bifurcated flow inside the cavity on the Rossiter loop by means of a joint time–frequency analysis of the pressure. The method used to compute the time–frequency spectrum is described in Larchevêque *et al.* (2004). The time step and the width of the sliding window are chosen to ensure a frequency resolution better than $St = 0.05$ according to the Gabor–Heisenberg principle of uncertainty. Note that only MIL$_l$ data are considered since this computation exhibits the largest duration for the non-bifurcated flow.

The resulting joint time–frequency pressure spectrum is plotted in figure 15(*a*) with a superimposed vertical dashed line denoting the bifurcation time identified from the time–wavenumber spectrum analysis. The plot shows that the first and second Rossiter modes are altered shortly after the bifurcation: their frequencies respectively decrease and increase to reach the values observed in figure 3 that are shown by solid horizontal lines in figure 15(*a*). Moreover, the harmonic of the first Rossiter mode appears for $t/T_{Rossiter} \gtrsim 30$ as shown by the dashed horizontal line corresponding to the second dominant peak of figure 3. A frequency bispectral analysis confirms that this mode originates in a quadratic interaction of the first Rossiter mode with itself.

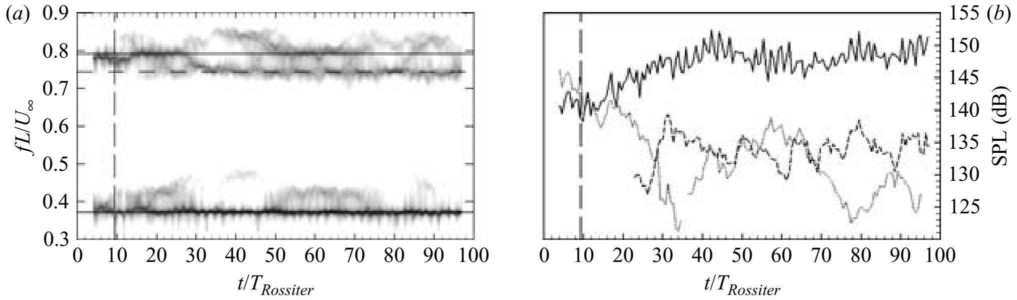

FIGURE 15. (*a*) Time–frequency spectrum of pressure at location ($x/L=0, z/L=-0.25$) from MIL$_l$ computation and (*b*) time evolution of peak sound pressure level for: ——, first Rossiter mode; ⋯⋯, second Rossiter mode and — — —, harmonic of first Rossiter mode when these modes are identified in the spectrum (*a*). Horizontal solid lines in (*a*) correspond respectively to the mean Strouhal numbers of the first and second Rossiter modes deduced from the frequency spectrum. Similarly, the dashed horizontal is related to the mean frequency of the harmonic of the first Rossiter mode. Vertical dashed line in (*a*) and (*b*) corresponds to the bifurcation time at location ($x=0, z=-L/4$) identified from a plot similar to the ones in figure 13. Note that the spectrum has been computed as a spanwise average over measurement points ranging from $y=0.2L$ to $y=2.2L$ to reduce noise level.

The instantaneous sound pressure levels of the three modes shown in figure 15(*a*) are computed as the maximal value for the local peaks encountered within intervals of width $St=\pm 0.03$ centred on the mean frequency of each mode. It is seen from figure 15(*b*) that before the bifurcation the second Rossiter mode is dominant whereas the harmonic of the first mode does not exist. These features, as well as the increased frequency for the first mode and the reduced frequency for the second mode in comparison with the steady bifurcated spectrum, make the non-bifurcated spectrum similar to the steady spectrum of the MS computation seen in figure 3(*c*). Such features are also shown by considering the pressure spectrum from the bifurcation-free MIL$_p$ computation.

Beyond the bifurcation time, the energy content of the first mode rises gradually to reach a plateau close to 150 dB, the harmonic of the first Rossiter mode appearing once the first mode has levelled. On the other hand the energy of the second mode globally decreases while being strongly modulated over large time with an amplitude larger than 15 dB. The regions of highly energetic second Rossiter mode, namely $20 \lesssim t/T_{Rossiter} \lesssim 25$ and $50 \lesssim t/T_{Rossiter} \lesssim 70$ closely match the regions exhibiting a peak of Strouhal number equal to 0.42 in figure 15(*a*), resulting from a quadratic interaction between the first and second Rossiter modes. Note that it is unlikely that the Rossiter loop is responsible for the bifurcation since the smooth evolution of the Rossiter modes follows the fast switching to the bifurcated configuration.

Finally, note that the pressure at frequencies of the first Rossiter mode and its harmonics is not the only quantity altered by the bifurcation. Frequency–wavenumber analysis not shown here for conciseness demonstrates that both vortical structures related to the first Rossiter mode and low-frequency velocity and pressure fluctuations are spanwise modulated by the bifurcation. While low-frequency phenomena are almost uniformly modulated over the whole cavity, spanwise modulation of the velocity fluctuations related to the first Rossiter mode are progressively damped away from the downstream corner, in contrast to pressure fluctuations. It is therefore suggested that the impingement of spanwise asymmetrically modulated vortices from the mixing layer generates spanwise twisted pressure waves that keep their bifurcated form over long distances while the vortices are rapidly smoothed after entering the cavity.

5. Conclusion

The computations carried out have clearly demonstrated that for the geometrical configuration and the flow parameters considered in this work the spanwise asymmetry of the mean flow originates in a bifurcation induced by the lateral walls of the cavity. Moreover, it has been found that the branch of the bifurcation can be selected by using a slightly non-symmetric incoming mean flow in the spanwise direction.

The aero–acoustic coupling responsible for the flow oscillations appears not to be directly involved in the bifurcation process. This idea is supported by the experimental visualizations of Maull & East (1963) for incompressible cavity flows with various widths that have highlighted spanwise cells similar to those observed in the present computations. The bifurcation, rather, emerges from an odd constraining of the natural wavelength of three-dimensional steady modulations by the width of the cavity. The effect of the spanwise extent on the bifurcation is beyond the scope of the present study. It is nonetheless worth noting that spanwise correlation lengths due to the unsteady turbulent structures in the mixing layer and the cavity are five to ten time smaller than the spanwise length. This implies that the bifurcation process may not be related to turbulence.

The origin of the modulations remains to be established. However it must be emphasized that some regions with large spanwise modulations have been found to roughly match regions which are potentially unstable to the centrifugal instability as identified using the generalized Rayleigh criterion defined by Sipp & Jacquin (2000). Experimental measurements by Beaudoin *et al.* (2004) on backward-facing step flow, as well as low-Reynolds-number linear stability studies by Albensoeder *et al.* (2001) for lid-driven cavities and Barkley *et al.* (2002) for backward-facing step flows, have highlighted the role of the centrifugal instability in the generation of three-dimensional structures in recirculating flows. However, as in the present study, some uncertainties remain because of slight differences in the location of the potential instability and that of the three-dimensional structures. Linear stability analysis of the present geometrical configuration (but for a laminar flow) could help to identify the origin of the modulations. The analysis of the bifurcation process itself by means of such low-Reynolds-number approach could be more difficult since the MS computation that exhibits the highest level of turbulent viscosity and consequently the lowest effective Reynolds number reduces the strength of the bifurcation, suggesting a possible Reynolds number dependence of this process. From a more global viewpoint, there is a possibility that as well as cavity, bifurcations may be encountered in flows such as the ones mentioned above where there are lateral geometrical constraints.

While not being involved in the bifurcation, the aero–acoustic coupling is altered by the quick transition to the bifurcated state. It induces a slower modulation of the energy content of the Rossiter modes, resulting after a few periods of oscillation in a switch of the dominant mode and an increase in nonlinear interactions between pressure modes. This evolution bears some resemblance to the ‘mode-switching’ phenomenon first described by Kegerise *et al.* (2004) that is characterized by a competitive energy exchange between Rossiter modes over a few periods. Analogously to the present results, the mode-switching may be caused by a transient modification of the flow field inside the cavity. Such unsteadiness is consistent with the variation over time of the vortex–downstream corner interaction as described by Rockwell &

Naudascher (1979) that yields a variation in the number of vortical structures entering the cavity and consequently results in a transient alteration of the recirculating bubble.

From an applied perspective, the sensitivity of the energy repartition among Rossiter modes to changes in the flow field inside the cavity should be taken into account when considering control devices, especially those of closed loop and/or active nature. Numerically the effective Reynolds number dependence of the bifurcation could prevent unsteady Reynolds-averaged computations or even detached-eddy simulations characterized by a high level of added turbulent viscosity from reproducing the bifurcation and its effect on the Rossiter loop. Therefore these kinds of method, which are widely used in industry, could result in severely wrong predictions of the local velocity if applied to the analysis of such bifurcated flows. Further work should consider that point in order to clarify it.

Drs N. Forestier and L. Jacquin are gratefully acknowledged for making their measurement database available as well as for numerous fruitful discussions dealing with the specific dynamics of the flow. The authors are also indebted to Professor P. Comte and Dr D. Sipp for their comments on some parts of this research work.

REFERENCES

Ahuja, K. K. & Mendoza, J. 1995 Effects of cavity dimensions, boundary layer, and temperature on cavity noise with emphasis on benchmark data to validate computational aeroacoustic codes. *Contractor Report* 4653. NASA.

Albensoeder, S., Kuhlmann, H. C. & Rath, H. J. 2001 Three-dimensional centrifugal-flow instabilities in the lid-driven-cavity problem. *Phys. Fluids* **13**, 121–135.

Barkley, D., Gabriela m. Gomes, M. & Henderson, R. D. 2002 Three-dimensional instability in flow over a backward-facing step. *J. Fluid. Mech.* **473**, 167–190.

Beaudoin, J.-F., Cadot, O., Aider, J.-L. & Wesfreid, J. E. 2004 Three-dimensional stationary flow over a backward-facing step. *Eur. J. Mech.* B **23**, 147–155.

Colonius, T. 2001 An overview of simulation, modeling, and active control of flow/acoustic resonance in open cavities. *AIAA Paper* 2001-0076.

Forestier, N., Geffroy, P. & Jacquin, L. 2000 Étude expérimentale des propriétés instationnaires d'une couche de mélange compressible sur une cavité : cas d'une cavité ouverte peu profonde. *Tech. Rep.* RT 22/00153 DAFE. ONERA (in French).

Forestier, N., Jacquin, L. & Geffroy, P. 2003 The mixing layer over a deep cavity at high-subsonic speed. *J. Fluid Mech.* **475**, 101–145.

Gharib, M. & Roshko, A. 1987 The effect of flow oscillations on cavity drag. *J. Fluid Mech.* **177**, 501–530.

Gloerfelt, X., Bailly, C. & Juvé, D. 2000 Calcul direct du rayonnement acoustique d'un coulement affleurant une cavit. *C. R. Acad. Sci. Paris* IIb **328**, 625–631.

Gloerfelt, X., Bogey, C., Bailly, C. & Juvé, D. 2002 Aerodynamic noise induced by laminar and turbulent boundary layers over rectangular cavities. *AIAA Paper* 2002-2476.

Hunt, J. C. R., Wray, A. A. & Moin, P. 1988 Eddies, stream, and convergence zones in turbulent flows. In *Proc. 1988 Summer Program*, pp. 193–208. CTR, Stanford.

Karamcheti, K. 1955 Acoustic radiation from two-dimensional rectangular cutouts in aerodynamic surfaces. *Tech. Note* 3487. NACA.

Kegerise, M. A., Spina, E. F., Garg, S. & Cattafesta III, L. N. 2004 Mode-switching and nonlinear effects in compressible flow over a cavity. *Phys. Fluids* **16**, 678–687.

Komerath, N. M., Ahuja, K. K. & Chambers, F. W. 1987 Prediction and measurement of flows over cavities - a survey. *AIAA Paper* 87-0166.

Larchevêque, L., Sagaut, P., Lê, T.-H. & Comte, P. 2004 Large-eddy simulation of a compressible flow in a three-dimensional open cavity at high reynolds number. *J. Fluid. Mech.* **516**, 265–301.

Larchevêque, L., Sagaut, P., Mary, I., Labbé, O. & Comte, P. 2003 Large-Eddy Simulation of a compressible flow past a deep cavity. *Phys. Fluids* **15**, 193–210.

Lenormand, E., Sagaut, P., Ta Phuoc, L. & Comte, P. 2000 Subgrid-scale models for Large-Eddy Simulation of compressible wall bounded flows. *AIAA J.* **38**, 1340–1350.

Lomb, N. R. 1976 Least-squares frequency analysis of unequally spaced data. *Astrophys. Space Sci.* **39**, 447–462.

Mary, I. & Sagaut, P. 2002 LES of a flow around an airfoil near stall. *AIAA J.* **40**, 1139–1145.

Maull, D. J. & East, L. F. 1963 Three-dimensional flow in cavities. *J. Fluid Mech.* **16**, 620–632.

Rizzetta, D. P. 1988 Numerical simulation of supersonic flow over a three dimensional cavity. *AIAA J.* **26**, 799–807.

Rockwell, D. & Knisely, C. 1980 Observations of the three-dimensional nature of unstable flow past a cavity. *Phys. Fluids* **23**, 425–431.

Rockwell, D. & Naudascher, E. 1978 Review – self-sustaining oscillations of flow past cavities. *Trans. ASME*: *J. Fluids Engng* **100**, 152–165.

Rockwell, D. & Naudascher, E. 1979 Self-sustained oscillations of impinging free shear layer. *Annu. Rev. Fluid Mech.* **11**, 67–94.

Roshko, A. 1955 Some measurements of flow in a rectangular cutout. *Tech. Note* 3488. NACA.

Rossiter, J. E. 1964 Wind-tunnel experiments on the flow over rectangular cavities at subsonic and transonic speeds. *Aero. Res. Counc. R&M* 3438.

Rowley, C. W., Colonius, T. & Basu, A. J. 2002 On self-sustained oscillations in two-dimensional compressible flow over rectangular cavities. *J. Fluid Mech.* **455**, 315–346.

Sagaut, P. 2005 *Large-eddy Simulation for Incompressible Flows – An Introduction*, 3rd Edn. Springer.

Sagaut, P., Garnier, E., Tromeur, E., Larchevêque, L. & Labourasse, E. 2004 Turbulent inflow conditions for large-eddy simulation of supersonic and subsonic wall flows. *AIAA J.* **42**, 469–477.

Scargle, J. D. 1982 Studies in astronomical time series II. statistical aspects of spectral analysis of unevenly spaced data. *Astrophys. J.* **263**, 835–853.

Shieh, C. M. & Morris, P. J. 2000 Parallel computational aeroacoustic simulation of turbulent subsonic cavity flow. *AIAA Paper* 2000-1914.

Sipp, D. & Jacquin, L. 2000 Three-dimensional centrifugal-type instabilities of two-dimensional flows in rotating systems. *Phys. Fluids* **12**, 1740–1748.

Stuart, J. T. 1967 On finite amplitude oscillations in laminar mixing layers. *J. Fluid Mech.* **29**, 417–440.

Suponitsky, V., Avital, E. & Gaster, M. 2005 On three-dimensionality and control of incompressible cavity flow. *Phys. Fluids* **17**, 104103.

Tracy, M. B. & Plentovich, E. B. 1997 Cavity unsteady-pressure measurements at subsonic and transonic speeds. *Technical Paper* 3669. NASA.